(Received 18 July 2025, Accepted 17 September 2025, Scheduled 17 October 2025)

Model of a Planar Cherenkov-Type Antenna for Microwave Applications

Vadym Pazynin[1], Kostyantyn Sirenko[2, *], and Wilhelm Keusgen[1]

[1] *Technical University of Berlin, Berlin, Germany*
[2] *O.Ya. Usikov Institute for Radiophysics and Electronics, National Academy of Sciences of Ukraine, Kharkiv, Ukraine*

ABSTRACT: In this paper, a radiator employing the Cherenkov mechanism for electromagnetic energy transfer from an optically less dense medium into a more dense one is developed and studied using a two-dimensional numerical model. The radiator's principal components are a dielectric prism and an open dielectric waveguide, where the phase velocity of waves exceeds that within the prism. For two linear polarizations in the 24 to 64 GHz range, and this radiator exhibits high efficiency (over 93%) and radiation patterns with main lobes that closely coincide in both direction and width. The direction of radiation demonstrates strong agreement with predictions from the Cherenkov wave theory and shows weak dependence on frequency. These characteristics make the developed antenna suitable for the directional emission and reception of electromagnetic pulses of various polarizations with spectral bandwidths of up to one octave or more. It is demonstrated that the radiation patterns of such antennas can be electrically controlled by altering the permittivity of the dielectric waveguide using an external control signal. The proposed antenna design avoids expensive fabrication processes and can be scaled to sub-millimeter wave ranges without significant modifications.

1. INTRODUCTION

When a charged particle travels at a speed exceeding the speed of light in the surrounding medium, it becomes a source of Cherenkov radiation [1–3]. This radiation is linearly polarized, anisotropic, and generated through a simple physical mechanism. The electric field of moving charged particle polarizes atoms of the medium along its trajectory. The subsequent depolarization of these atoms leads to the emission of secondary waves and their interference. When the mentioned condition on the charged particle's speed is met, the interference of all waves emitted by the polarized atoms results in the formation of Cherenkov wavefronts in the form of Mach cones. The particle's kinetic energy is thereby converted into the energy of outgoing electromagnetic waves. This effect finds its use in a wide range of fields, including particle physics and astrophysics experiments [4], nuclear power engineering [5], and biomedical applications such as radiotherapy and imaging [6]. The energy transfer is also possible in the opposite direction, from electromagnetic waves to charged particles. This phenomenon is known as inverse Cherenkov effect and is widely used in the development of compact charged particle accelerators [7].

The same effect can be realized without a charged particle [8–11]. In this scenario, the field that polarizes atoms of the medium originates from a wave propagating in an open waveguiding structure, such as an open dielectric waveguide. The fields of such waves are not strictly confined within the waveguide but partially extend beyond it. This part of the wave decays exponentially with distance from the waveguide and travels along the waveguide together with the main part of the wave. If this evanescent wave encounters another medium where the speed of light is lower than its own speed (Fig. 1), the same polarization mechanism for generating Cherenkov waves occurs. The energy of the primary guided wave is transferred into the optically more dense medium, from which it can be subsequently emitted into free space. This phenomenon can be considered as a wave analog [12–14] of the "classic" Cherenkov effect [15–18], and it forms the basis for the development of Cherenkov-type antennas [8–11]. It should be noted here that a similar effect of Cherenkov radiation generation is also theoretically predicted for electrodynamic systems without a feeding waveguide [19, 20], i.e., for pulse waves propagating in homogeneous media. However, in this case, strict requirements are imposed on the frequency, spatial, and energy characteristics of both the primary pulse and the medium.

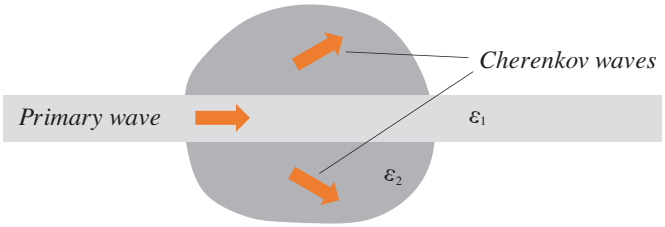

FIGURE 1. Schematic illustration of the surface-to-volume wave conversion in a Cherenkov radiator. $\varepsilon_2 > \varepsilon_1$.

The reciprocity theorem [21, 22] ensures that this energy transfer process can also occur in the reverse direction, from an optically more dense medium into a less dense one (wave analog of inverse Cherenkov effect). This principle is employed in prism couplers, which are used to lead light energy into thin

* Corresponding author: Kostyantyn Sirenko (SirenkoKY@nas.gov.ua).

dielectric films [23]. In such cases, the energy transfer between media can also be physically explained "*...by partially frustrating the total internal reflection and by distributed coupling.*" ([23], p. 149). Despite being accurate, this explanation is not as elegant as the one offered by the Cherenkov wave theory.

Despite simplicity of the concept of converting surface (guided) waves into volumetric ones, radiators based on this principle have not seen widespread development yet. This is likely because such devices require a dielectric filling of a volume whose linear dimensions are tens of times larger than the operating wavelength. In the most common microwave bands (with wavelengths in the order of centimeters), this requirement leads to antenna designs with unfavorable size and weight characteristics. However, shifting towards higher-frequency bands, this drawback becomes less significant, and factors such as efficiency, directivity, and broadband operation take precedence. Since the polarization (Cherenkov) mechanism of energy transfer between media is possible at any wavelength where the macroscopic averaging of material parameters is applicable, it is reasonable to expect that Cherenkov-type antennas will find their niche for applications in the millimeter and submillimeter wave ranges. This statement can be partly supported by works [24–26], where structures similar to that shown in Fig. 1 are used to convert infrared pulses propagating in a dielectric waveguide with nonlinear permittivity into terahertz waves and their subsequent radiation into free space by generating Cherenkov waves.

The current study aims to investigate fundamental wave phenomena occurring in Cherenkov-type antennas and assess their potential for practical applications. We focus on three main aspects of their functioning: broadband performance, polarization sensitivity, and the ability to manipulate radiation.

Previous studies [8–11] on Cherenkov-type antennas clearly explain the physical mechanism of their functioning and provide assessments of their basic characteristics. However, despite the use of pulse excitation in their model prototypes, the characteristics calculated by the authors (efficiency, radiation pattern [10, 11]) were obtained only for narrow frequency ranges. On the other hand, work [9] demonstrates the possibility of emitting a short pulse (with a duration much shorter than the propagation time along the antenna) as a pulse wave with a wide (of the order of the antenna aperture size) and nearly plane wavefront. This gives reason to expect broadband behavior of such radiators, in particular a weak dependence of the radiation direction on frequency.

Another issue that, in our opinion, requires clarification concerns the polarization sensitivity of Cherenkov-type antennas. Works [8–11] demonstrate promising results of modelling the radiation of waves with different polarizations, which allows us to assume that Cherenkov antennas are highly efficient for two orthogonal polarizations. However, the difference in the phase velocities of E- and H-waves in a dielectric waveguide can lead to significant differences in the corresponding frequency dependencies of antenna efficiency and directivity. Therefore, a comparison of these characteristics for the two polarizations in a single antenna should be performed.

Finally, the specific dependence of the radiation direction of Cherenkov-type antennas on the phase velocity of the primary wave in a dielectric waveguide allows us to expect the possibility of tuning their radiation patterns by changing this phase velocity. Assessing this possibility is also important for the further development of such antennas.

We employ numerical simulation, focusing primarily on the microwave frequency range, while keeping in mind that all geometric parameters of the analyzed structures can be scaled for the operation at shorter wavelengths. To calculate all electrodynamic characteristics presented in this work, the method of exact absorbing conditions (EACs) was used [27–33]. EAC method is based on a mathematically rigorous transformation of initial boundary value problems in open (unbounded, extending to infinity) domains into their equivalent counterparts in closed domains bounded by virtual boundaries with EACs on them. These problems are then solved numerically. In this work, finite-difference time-domain (FDTD) method [34] was used, although other numerical methods (e.g., DG-FEM [32]) may also be applied. EAC method has proven to be a reliable, highly efficient, and relatively simple tool for modeling transient processes in the time domain. The use of EACs on virtual boundaries enclosing a domain of computation prevents the reflection of outgoing waves from these boundaries, as if they were fully absorbed by these boundaries (hence the name "absorbing"), thus, effectively simulating outgoing waves' undisturbed propagation to infinity. This property is independent of the temporal duration of simulated processes, which is particularly crucial when analyzing resonant situations. This distinguishes EAC method from mathematically non-rigorous alternatives [35], such as those based on perfectly matched layers (PML, see [34]).

The paper is organized as follows. In Section 2, we briefly formulate the initial boundary value problems considered in this work and explain main stages of our numerical experiments. Section 3 presents the results of preliminary numerical experiments that are essential for the subsequent model synthesis of the Cherenkov radiator. Section 4 provides results of this synthesis, including energy and spatial-frequency characteristics of the Cherenkov antenna for two linear polarizations. In Section 5, the possibility of creating a beam-steering Cherenkov antenna is investigated.

2. EAC METHOD AS A TOOL FOR NUMERICAL EXPERIMENTS

We consider initial boundary value problems that describe the evolution of pulsed E- and H-waves in analysis domains $\mathbf{Q_L}$, which represent a fragment of the Cartesian plane $\{y, z\}$ bounded by rectangular virtual boundary $\mathbf{L}$, see Fig. 2. This boundary encloses all field sources and scatterers essential for models under study. The geometry and number of scatterers, in general, can be arbitrary and are defined based on a specific structure being modeled. The only constraint is that an entire modeled structure and electromagnetic field are independent of the coordinate x. In addition, structures considered in this work include one or two waveguide ports, which, being finite geometry-wise (Fig. 2), mimic the behavior of semi-

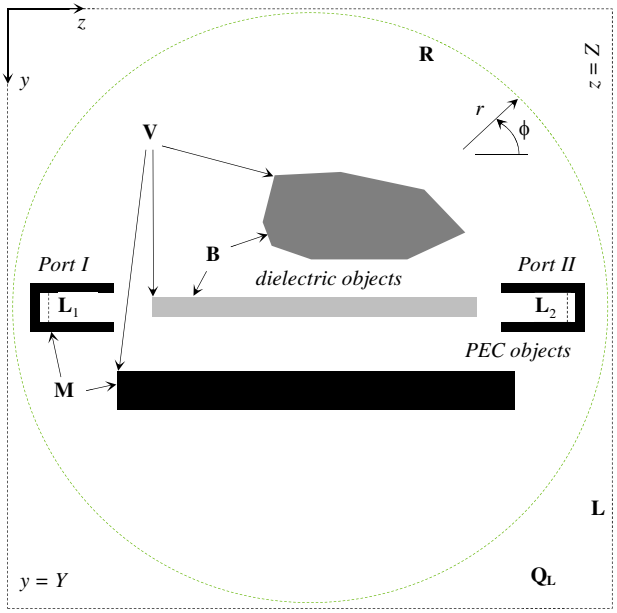

FIGURE 2. General view of the analysis domain. Projections of metal elements onto the plane $\{y, z\}$ are shown in black, and dielectric elements in gray. Black dashed lines represent virtual boundaries. Green dashed line is the reference circle **R** inside the computation domain for radiation pattern finding.

infinite, plane-parallel waveguides [33]. At cross-sections of these waveguide ports, the analysis domain $\mathbf{Q_L}$ is bounded by virtual boundaries $\mathbf{L}_p$, where p is the port number. Electromagnetic energy may enter the domain $\mathbf{Q_L}$ (as incident waves) or exit it (as scattered or reflected waves) through these ports.

For E-waves ($E_x, H_y, H_z \neq 0$), the initial boundary value problem is as follows

$$
\begin{cases}
\dfrac{\varepsilon}{\eta_0}\dfrac{\partial E_x}{\partial t} = \dfrac{\partial H_z}{\partial y} - \dfrac{\partial H_y}{\partial z} - \sigma E_x, \\
\eta_0\dfrac{\partial H_y}{\partial t} = -\dfrac{\partial E_x}{\partial z}, \quad \eta_0\dfrac{\partial H_z}{\partial t} = \dfrac{\partial E_x}{\partial y}, \\
\quad t = ct' \quad t \geq 0, \quad g \equiv \{y, z\} \in \mathbf{Q_L}, \\
E_x\,(g, 0) = H_y\,(g, 0) = H_z\,(g, 0) = 0, \\
\partial E_x(g, 0)/\partial t = \partial H_y(g, 0)/\partial t = \partial H_z(g, 0)/\partial t = 0, \\
E_x\,(g, t)\,\big|_{g\in\mathbf{M}} = 0, \\
E_x^{(i)}\,(g, t)\,\big|_{g\in\mathbf{B}} = E_x^{(j)}\,(g, t)\,\big|_{g\in\mathbf{B}}, \\
H_{tan}^{(i)}\,(g, t)\,\big|_{g\in\mathbf{B}} = H_{tan}^{(j)}\,(g, t)\,\big|_{g\in\mathbf{B}}, \\
\int\limits_V (\varepsilon E_x^2 + H_y^2 + H_z^2)dV < \infty, \\
\dfrac{\partial u_m^{(p)}(z, t)}{\partial z} = \mp\dfrac{\partial u_m^{(p)}(z, t)}{\partial t} \\
\qquad\qquad \mp\lambda_m^{(p)} \int\limits_0^t u_m^{(p)}(z, \tau)K_m^{(p)}(t - \tau)d\tau, \quad p = 1, 2, \\
\quad E_{x,out}^{(p)}(g, t)\big|_{g\in\mathbf{L}_p} = \sum\limits_{m=1}^{\infty} u_{m,out}^{(p)}(z, t)\big|_{\mathbf{L}_p} \cdot \mu_m^{(p)}(y), \\
\quad E_{x,inc}^{(1)}(g, t)\big|_{g\in\mathbf{L}_1} = u_{n,inc}^{(1)}(z, t)\big|_{g\in\mathbf{L}_1} \cdot \mu_n^{(1)}(y), \\
\mathbf{A_L}\big[E_{x,out}(g, t)\big]_{g\in\mathbf{L}} = 0.
\end{cases}
\tag{1}
$$

For H-waves ($H_x, E_y, E_z \neq 0$)

$$
\begin{cases}
\eta_0\dfrac{\partial H_x}{\partial t} = -\Big(\dfrac{\partial E_z}{\partial y} - \dfrac{\partial E_y}{\partial z}\Big), \\
\dfrac{\varepsilon}{\eta_0}\dfrac{\partial E_y}{\partial t} = \dfrac{\partial H_x}{\partial z} - \sigma E_y, \quad \dfrac{\varepsilon}{\eta_0}\dfrac{\partial E_z}{\partial t} = -\dfrac{\partial H_x}{\partial y} - \sigma E_z, \\
\quad t = ct' \quad t \geq 0, \quad g \equiv \{y, z\} \in \mathbf{Q_L}, \\
H_x\,(g, 0) = E_y\,(g, 0) = E_z\,(g, 0) = 0, \\
\partial H_x(g, 0)/\partial t = \partial E_y(g, 0)/\partial t = \partial E_z(g, 0)/\partial t = 0, \\
E_{tan}\,(g, t)\,\big|_{g\in\mathbf{M}} = 0, \\
E_{tan}^{(i)}\,(g, t)\,\big|_{g\in\mathbf{B}} = E_{tan}^{(j)}\,(g, t)\,\big|_{g\in\mathbf{B}}, \\
H_x^{(i)}\,(g, t)\,\big|_{g\in\mathbf{B}} = H_x^{(j)}\,(g, t)\,\big|_{g\in\mathbf{B}}, \\
\int\limits_V \big(H_x^2 + \varepsilon(E_y^2 + E_z^2)\big)dV < \infty, \\
\dfrac{\partial u_m^{(p)}(z, t)}{\partial z} = \mp\dfrac{\partial u_m^{(p)}(z, t)}{\partial t} \\
\qquad\qquad \mp\lambda_m^{(p)} \int\limits_0^t u_m^{(p)}(z, \tau)K_m^{(p)}(t - \tau)d\tau, \quad p = 1, 2, \\
\quad H_{x,out}^{(p)}(g, t)\big|_{g\in\mathbf{L}_p} = \sum\limits_{m=0}^{\infty} u_{m,out}^{(p)}(z, t)\big|_{\mathbf{L}_p} \cdot \mu_m^{(p)}(y), \\
\quad H_{x,inc}^{(1)}(g, t)\big|_{g\in\mathbf{L}_1} = u_{n,inc}^{(1)}(z, t)\big|_{g\in\mathbf{L}_1} \cdot \mu_n^{(1)}(y), \\
\mathbf{A_L}\big[H_{x,out}(g, t)\big]_{g\in\mathbf{L}} = 0.
\end{cases}
\tag{2}
$$

Here, E_x, E_y, E_z and H_x, H_y, H_z are Cartesian components of electric and magnetic field vectors $\vec{E} = \vec{E}(y, z, t)$ and $\vec{H} = \vec{H}(y, z, t)$; ε and σ denote the relative permittivity and specific conductivity; **B** and **M** represent the projections of three-dimensional surfaces of dielectric and metal objects onto the plane $\{y, z\}$, while points **V** represent the projections of metal and dielectric objects' edges onto $\{y, z\}$ (V is an arbitrary finite region that includes point **V**); t' is the time variable; $c = 299\,792\,458$ m/s is the speed of light in vacuum; $\eta_0 = \sqrt{\mu_0/\varepsilon_0} = \mu_0 c = 376.730\ldots$ Ohm is the impedance of free space, with $\mu_0 \approx 4\pi \times 10^{-7}$ H/m and $\varepsilon_0 \approx 8.854\,187\,8 \times 10^{-12}$ F/m being magnetic and electric constants. The international system of units (SI) is assumed, and the relative magnetic permeability $\mu \equiv 1$ for all considered objects.

The mathematical content of problems (1) and (2) is fairly straightforward. The first two lines in (1) and (2) are Maxwell's equations for the non-zero field components at each polarization. The third lines define domains of the definition of independent variables y, z, and t. The fourth and fifth lines specify trivial initial conditions. The sixth, seventh, and eighth lines are boundary conditions on surfaces of metal and dielectric objects (with i, j denoting their respective indices). The ninth lines define the conditions at edges [36, 37]. The remaining lines in (1) and (2) represent the exact absorbing conditions on virtual boundaries $\mathbf{L}_p$ and $\mathbf{L}$, which form the core of EAC method.

For waveguide ports, these conditions are applied to space-time amplitudes $u_m^{(p)}(z, t) \equiv u_{m,out}^{(p)}(z, t)$ [27–31] of outgoing waves at virtual boundaries $\mathbf{L}_p$. These conditions are convolutions of the space-time amplitudes' values on boundaries $\mathbf{L}_p$ at all previous moments of time with the kernel $K_m^{(p)}(t) = J_1(\lambda_m^{(p)}t)/t$. Here, J_1 is the Bessel function; $\lambda_m^{(p)} = m\pi/a^{(p)}$ are eigenvalues of plane-parallel waveguides (p is the waveguide number); $a^{(p)} = y_1^{(p)} - y_0^{(p)}$ is their

width; $y_0^{(p)}$, $y_1^{(p)}$ are coordinates of their walls. Regardless of the waveguide port, the upper sign in these convolutions corresponds to waves propagating in the direction of increasing z, while the lower sign corresponds to waves propagating in the direction of decreasing z.

The same convolution is used to find the longitudinal derivative $\partial u^{(1)}_{n,inc}(z,t)/\partial z$ of space-time amplitude $u^{(1)}_{n,inc}(z,t)$ of the primary (excitation) wave. We assume that it is defined only at port I on the boundary $\mathbf{L}_1$. The combination of functions $u^{(1)}_{n,inc}(z,t)$ and $\partial u^{(1)}_{n,inc}(z,t)/\partial z$ allows us to correctly embed pulse primary waves into the initial boundary value problems (1) and (2) and avoid problems associated with incorporating such primary waves into difference schemes equipped with PML [34].

The system of eigenfunctions $\mu_m^{(p)}(y)$ for plane-parallel waveguides is defined as

$$\mu_m^{(p)}(y) = \sqrt{2/a^{(p)}}\sin(\lambda_m(y-y_0^{(p)})), \quad m \geq 1 \tag{3}$$

for E-waves, and as

$$\mu_m^{(p)}(y) = \begin{cases} \sqrt{1/a^{(p)}}, & m = 0 \\ \sqrt{2/a^{(p)}}\cos(\lambda_m(y-y_0^{(p)})), & m > 0 \end{cases} \tag{4}$$

for H-waves. The set of functions $\mu_m^{(p)}(y)$ forms an orthonormal basis with the scalar product

$$\left(\mu_m^{(p)}(y), \mu_n^{(p)}(y)\right) \equiv \int_{y_0^{(p)}}^{y_1^{(p)}} \mu_m^{(p)}(y)\mu_n^{(p)}(y)dy = \begin{cases} 1, m = n \\ 0, m \neq n \end{cases} \tag{5}$$

and

$$u_m^{(p)}(z,t) = \left(U_x(y,z,t), \mu_m^{(p)}(y)\right), \tag{6}$$

where

$$U_x(y,z,t) \equiv \begin{cases} E_x(y,z,t), & \text{for } E\text{-waves} \\ H_x(y,z,t), & \text{for } H\text{-waves.} \end{cases} \tag{7}$$

The operator $\mathbf{A}_\mathbf{L}[\dots]$ formally represents EAC on the rectangular virtual boundary $\mathbf{L}$. This EAC is formulated for the x component of the outgoing wave's field $U_x(y,z,t)$ at this boundary. This component is obtained as the solution to the following auxiliary initial boundary value problems on each straight segment of the boundary $\mathbf{L}$ [28, 29]:

$$\begin{cases} U_x(y,z_i,t) = -\dfrac{2}{\pi}\displaystyle\int_0^{\pi/2}\frac{\partial V_z}{\partial t}d\varphi, \\ \dfrac{\partial^2 V_z}{\partial t^2} - \sin^2\varphi\dfrac{\partial^2 V_z}{\partial y^2} = \pm\dfrac{\partial U_x}{\partial z}, \quad \left\{\begin{matrix} z_i=Z \\ z_i=0 \end{matrix}\right\}, \\ V_z\big|_{t=0} = \partial V_z/\partial t\big|_{t=0} = 0 \end{cases} \tag{8}$$

$$\begin{cases} U_x(y_i,z,t) = -\dfrac{2}{\pi}\displaystyle\int_0^{\pi/2}\frac{\partial V_y}{\partial t}d\varphi, \\ \dfrac{\partial^2 V_y}{\partial t^2} - \sin^2\varphi\dfrac{\partial^2 V_y}{\partial z^2} = \pm\dfrac{\partial U_x}{\partial y}, \quad \left\{\begin{matrix} y_i=Y \\ y_i=0 \end{matrix}\right\}. \\ V_y\big|_{t=0} = \partial V_y/\partial t\big|_{t=0} = 0 \end{cases} \tag{9}$$

Here, $V_y = V_y(z,t,\phi;y_i)$ and $V_z = V_z(y,t,\phi;z_i)$ are auxiliary functions; y_i and z_i are parameters specifying the straight segment of the virtual boundary on which the corresponding function is defined. At corners of boundary $\mathbf{L}$, functions V_y and V_z are related by the following expression:

$$\begin{cases} \dfrac{\partial V_z}{\partial t} + \sin\varphi\dfrac{\partial V_z}{\partial y} = \mp\displaystyle\int_0^{\pi/2} R(\varphi,\varphi')\frac{\partial V_y}{\partial z}d\varphi' \quad \left\{\begin{matrix} z=Z \\ z=0 \end{matrix}\right\}, \\ \dfrac{\partial V_y}{\partial t} + \sin\varphi\dfrac{\partial V_y}{\partial z} = \mp\displaystyle\int_0^{\pi/2} R(\varphi,\varphi')\frac{\partial V_z}{\partial y}d\varphi' \quad \left\{\begin{matrix} y=Y \\ y=0 \end{matrix}\right\}, \end{cases} \tag{10}$$

where

$$R(\varphi,\varphi') = \frac{\sin^2\varphi'}{\sin^2\varphi + \sin^2\varphi'\cos^2\varphi}. \tag{11}$$

Once the geometry of objects of interest and the temporal profile of incident wave amplitude $u^{(p)}_{n,inc}(z,t)$ (including its number n) are specified, problems (1)–(11) describe the space-time transformations of pulsed E- and H-waves within the analysis domain $\mathbf{Q}_\mathbf{L}$. Their solutions represent nontrivial components of the electromagnetic field in $\mathbf{Q}_\mathbf{L}$ as functions of Cartesian coordinates y, z and time variable t.

In numerical experiments conducted in this work, these solutions were obtained using the FDTD method with a standard second-order accurate difference scheme and a staircase approximation of physical objects' boundaries [34]. The time interval for simulating transient processes was selected individually for each problem, based on its specifics and goals of a particular numerical experiment. In most cases, the natural limiting factor for this time interval is the requirement that the total electromagnetic energy within the entire computation domain is reduced to a negligibly small level compared to its maximum value.

The solutions to the initial boundary value problems described above were obtained using the custom-made software developed by the authors. It is a Windows® desktop application, which incorporates performance optimization through parallel processing across multiple (typically 5 to 20) threads. In addition, the computation of convolutions, which are present in EAC for waveguide ports (see (1), line 10), is optimized using the fast Fourier transform algorithm [28, 33].

Besides the field components' values themselves, it is also possible to compute integral characteristics of structures under study. In this work, we have used the following ones:

- $\tilde{U}_x(k)\big|_{P_i}$ — the Fourier spectrum of the field at a fixed observation point P_i inside the computation domain. Here, U_x is the x component of the field (as defined in equation (7)), and tilde "$\sim$" denotes the Fourier image of a function $U_x(t)$, as described below.

- Frequency-dependent energy reflection and transmission coefficients of the primary wave from a feeding port through a structure under study [28]:

$$R_{mn}(k) = \frac{\left|\tilde{u}^{(p)}_{m,out}(z_p,k)\right|^2}{\left|\tilde{u}^{(p)}_{n,inc}(z_p,k)\right|^2}\frac{\operatorname{Re}\Gamma^{(p)}_m}{\Gamma^{(p)}_n}, \quad k > \tilde{k}^{(p)}_n, \tag{12}$$

$$T_{mn}(k) = \frac{\left|\tilde{u}^{(q)}_{m,out}(z_q,k)\right|^2}{\left|\tilde{u}^{(p)}_{n,inc}(z_p,k)\right|^2}\frac{\operatorname{Re}\Gamma^{(q)}_m}{\Gamma^{(p)}_n}, \quad k > \tilde{k}^{(p)}_n. \quad (13)$$

Here, p is the number of waveguide port from which the primary wave arrives ($p = 1$, as mentioned above); its amplitude is $\tilde{u}^{(p)}_{n,inc}(z_p,k)$, and the mode number is n; q is the number of port into which the scattered wave exits; its amplitude is $\tilde{u}^{(q)}_{m,out}(z_q,k)$, and the mode number is m; $\Gamma^{(p)}_n(k) = \sqrt{k^2 - \left(\tilde{k}^{(p)}_n\right)^2}$; $\tilde{k}^{(p)}_n$ represents the cut-off wavenumber for the n-th mode of the p-th port. In all initial boundary value problems considered in this work, all ports are aligned along the z-axis (Fig. 2), and z_p, z_q are the corresponding coordinates of virtual boundaries.

- Antenna radiation pattern [27, 28]

$$D(\phi,k) = \lim_{r\to\infty}\frac{\left|\tilde{U}_x(r,\phi,k)\right|^2}{\max\limits_{0\le\phi\le 2\pi}\left|\tilde{U}_x(r,\phi,k)\right|^2}. \quad (14)$$

This limit is computed using the asymptotic representation of the Hankel function $H^{(1)}_m(\cdots)$ in the expansion of the x component of field $\tilde{U}_x(r,\phi,k) = \sum_{m=-\infty}^{m=\infty} a_m(k)H^{(1)}_m(kr)e^{im\phi}$ [28] into angular harmonics in free space (area outside the reference circle **R**, see Fig. 2).

- Poynting vector flux through the contour L

$$S_L(t) = \begin{cases}\int_L E_x(g,t)H_{tan}(g,t)dl, & \text{for } E\text{-waves}\\ \int_L E_{tan}(g,t)H_x(g,t)dl, & \text{for } H\text{-waves}\end{cases} \quad (15)$$

and its antiderivative with respect to the time variable

$$W_L(t) = \int_0^t S_L(\tau)d\tau. \quad (16)$$

The first three of the aforementioned characteristics imply the conversion of data from time domain to frequency domain. For this purpose, we use integral Fourier transform, which relates a given function $f(t)$ to its Fourier image $\tilde{f}(k)$:

$$\tilde{f}(k) = (2\pi)^{-1}\int_{-\infty}^{\infty} f(t)e^{ikt}dt, \quad (17)$$

$$f(t) = \int_{-\infty}^{\infty}\tilde{f}(k)e^{-ikt}dk. \quad (18)$$

Since in (1) and (2) the variable substitution $t = ct'$ was made (t is measured in meters), the unit of measurement for the Fourier spectrum $\tilde{f}(k)$ is "u·m", where "u" is the unit of measurement of $f(t)$. E.g., in the case of E-waves, the units of measurement for $U_x(t)$, $\tilde{U}_x(k)$, $u_n(t)$, and $\tilde{u}_n(k)$ are "V/m", "V", "V·m$^{-1/2}$", and "V·m$^{1/2}$", respectively.

The research methodology utilizing the initial boundary value problems described above can be broadly outlined as follows: (i) setting object of interest's geometry and electrodynamic parameters; (ii) simulating its response when excited by a pulse with the spectral width corresponding to a desired frequency band; (iii) converting time-domain data into the frequency domain and computing integral characteristics; (iv) modeling the object's response when excited by a narrowband (quasi-monochromatic) pulse. The subsequent sections present the results of numerical experiments conducted using this methodology.

3. PRELIMINARY NUMERICAL RESULTS

Before constructing a Cherenkov radiator, we need to address several auxiliary tasks related to its general design and functionality.

First of all, we secure the ability to connect the proposed antenna to a standard waveguide, for example, WR28 with a broad wall of $a = 7.1$ mm. Since antenna construction involves energy exchange between a dielectric waveguide and a dielectric object located in its near field, it is essential to define their permittivities and address the issue of coupling waveguides of different types. For the waveguide transmission line, a dielectric with $\varepsilon_1 = 2.2$ and $\tan\delta_1 = 10^{-4}$ (Teflon, cyclic olefin copolymer [38] or polyethylene [39]) was used, and for the Cherenkov scatterer, a dielectric with $\varepsilon_2 = 2.6$ and $\tan\delta_2 = 10^{-4}$ (polymethyl methacrylate or polystyrene [39]) was chosen.

To couple two different types of waveguides, we employ a simple approach based on the gradual transformation of the cross-section of transmission line. First, a wedge-shaped matcher for the transition from a standard WR28 waveguide to an identical waveguide filled with the dielectric with ε_1 is utilized, see Fig. 3(a). Second, this coupling section is extended with a horn-shaped expansion of metal walls and a transition to an open dielectric waveguide above a metal screen, see Fig. 3(b). The metal screen allows to limit the subsequent analysis to the upper half-space only, while the gap between the screen and dielectric waveguide helps to reduce undesirable radiation losses.

The reflection coefficient from this matcher is less than –20 dB across the frequency range from 24 GHz to at least 64 GHz, see Fig. 3(c). This ensures that the reflection of the primary TE_1 wave from such a waveguide discontinuity can be neglected throughout the entire frequency range of interest. In our study, this range covers only the propagation regions of the first and second eigenmodes of WR28 waveguide ($\tilde{k}_1 \le k \le \tilde{k}_3$, where $\tilde{k}_1 \approx 442.4778\,\text{m}^{-1}$, $\tilde{k}_2 = 2\tilde{k}_1$, $\tilde{k}_3 = 3\tilde{k}_1$ are the waveguide's first three modes' cut-off wavenumbers, which correspond to cut-off frequencies $\tilde{f}_1 \approx 21.1121$ GHz, $\tilde{f}_2 = 2\tilde{f}_1$, $\tilde{f}_3 = 3\tilde{f}_1$). The values of $\tilde{k}_2$ and $\tilde{k}_3$ are marked by the vertical dashed lines in Fig. 3(c).

Our first numerical experiment aimed to evaluate the main spatial and energy characteristics of the Cherenkov wave generation process. We used two identical matchers (Fig. 3(b)) connected by a regular section of dielectric waveguide. When the dielectric waveguide is excited by a primary wave from one of the ports, this two-port configuration allows to calculate the energy balance and to estimate the portion of energy extracted from the dielectric waveguide and radiated into free space.

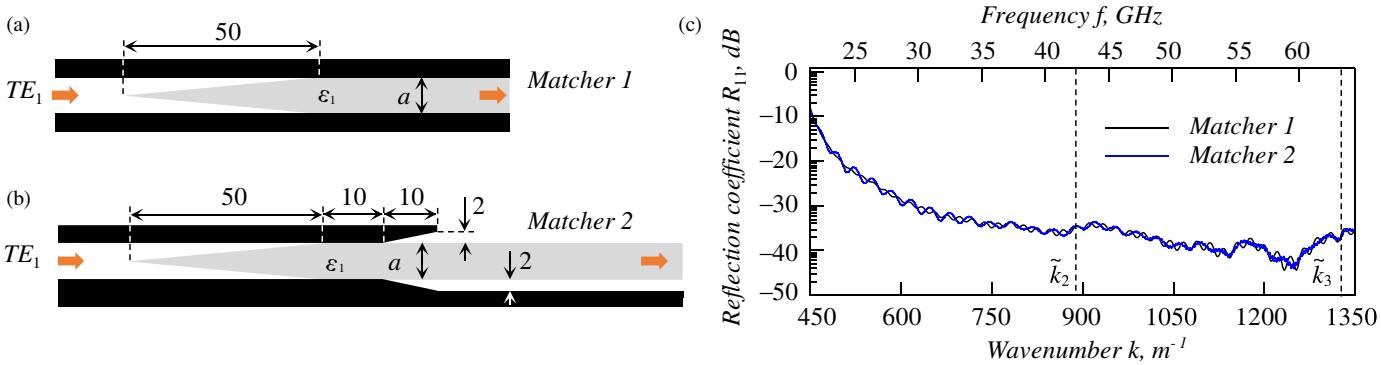

FIGURE 3. (a), (b) Two matchers used for coupling the Cherenkov radiator with WR28 waveguide. (c) Reflection coefficient R_{11} of TE_1 wave back into the same mode of the same waveguide from these matchers. All dimensions are in millimeters.

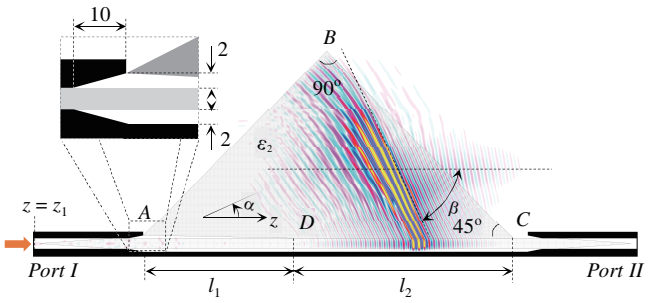

FIGURE 4. Geometry of the problem demonstrating Cherenkov radiation of a broadband pulse in the system "open dielectric waveguide + dielectric prism". The distribution of E_x component in the computation domain is shown for the instant of time $t' = 1.8\,\mathrm{ns}$.

As the object where Cherenkov waves are generated, we used a quadrilateral prism $ABCD$ with angles 90° and 45° and permittivity ε_2, see Fig. 4. Its face CD lies on the surface of the dielectric waveguide and has a length of $l_2 = 150$ mm. Its face AD forms a triangular gap with the dielectric waveguide. The length of the projection of this face onto the longitudinal z-axis is $l_1 = 100\,\mathrm{mm}$, and the distance from vertex A to the waveguide surface is 2 mm.

In general, this gap between the prism and waveguide is not strictly necessary, Cherenkov radiation would still occur if the prism is in full contact with the waveguide surface. In this aspect, we follow [23], where the use of such a gap (or a gradual reduction of the distance between the waveguide and the prism) is recommended (in reception mode) to achieve a more uniform output in the dielectric waveguide. In the context of the radiator being developed here, this gap allows (in emission mode) to control the spatial distribution of energy in a radiated pulse, aiming for a more uniform distribution in directions perpendicular to the wave vector.

Our experiment involved modeling the formation and radiation of a pulsed Cherenkov wave by the system "open dielectric waveguide + dielectric prism", see Fig. 4. The primary wave is a pulsed TE_1 wave from port I. Its time profile was defined by the function

$$u^{(1)}_{n,inc}(z,t) = 4{\cdot}S(t)\cdot\cos\big(k_c(t-T)\big)\frac{\sin\big(k_s(t-T)\big)}{t-T}, \quad (19)$$

where

$$S(t) = \tilde{x}^2(t)\cdot(3-2\tilde{x}(t)), \quad (20)$$

$$\tilde{x}(t) = \begin{cases} (t-t_0)/(T-t_0), & t_0 \le t \le T \\ (t-t_1)/(T-t_1), & T \le t \le t_1 \\ 0, & t<0,\ t>t_1 \end{cases}, \quad (21)$$

which is set in the cross-section $z = z_1$ located 3.5 mm from the tip of the wedge-shaped matcher (Fig. 3(b)). The following values of the parameters were used: $n = 1$ (TE_1 wave), $t_0 = 0$, $t_1 = 0.3\,\mathrm{m}$ (approximately 1 ns), $T = (t_0+t_1)/2 = 1.5\,\mathrm{m}$, $k_c = 900\,\mathrm{m}^{-1}$, $k_s = 450\,\mathrm{m}^{-1}$. Fig. 5(a) plots this excitation's time profile; its amplitude spectrum $\left|\tilde{u}^{(1)}_{1,inc}(k)\right|$ is approximately equal to 1 across the entire studied frequency range, Fig. 5(b).

The radiation of such a pulse was simulated under the assumption of lossless dielectric elements ($\tan\delta_1 = \tan\delta_2 = 0$). It demonstrated exceptionally high efficiency for this process, nearly all the input energy was radiated into free space as a compact electromagnetic pulse. It had a longitudinal spatial dimension (along the wave vector) corresponding to the duration of excitation (1 ns), and a transverse dimension significantly exceeded the feeding waveguide's width a.

The reflection coefficient of the primary wave back into port I, R_{mn}, and its transmission coefficient into port II, T_{mn}, as functions of the frequency parameter k, are negligibly small, as shown in Fig. 6. The same figure also plots the frequency dependent radiation efficiency coefficient

$$\zeta(k) = 1 - R_{11}(k) - R_{21}(k) - R_{31}(k) \\ -T_{11}(k) - T_{21}(k) - T_{31}(k). \quad (22)$$

This function represents the fraction of the primary wave's energy that is radiated, which exceeds 0.99 in the range from $k = 504.2\,\mathrm{m}^{-1}$ to $k = 1168.2\,\mathrm{m}^{-1}$ (24.0571 to 55.7389 GHz). A gradual decrease of $\zeta(k)$ with increasing k ($\zeta \approx 0.97$ for $k = 1350\,\mathrm{m}^{-1}$) reflects the fact that at higher frequencies, a smaller portion of the waveguide wave propagates outside the waveguide and interacts with the external dielectric prism. This characteristic can be improved by increasing the length of the wave-prism interaction section, or in other words, the length of the prism face CD.

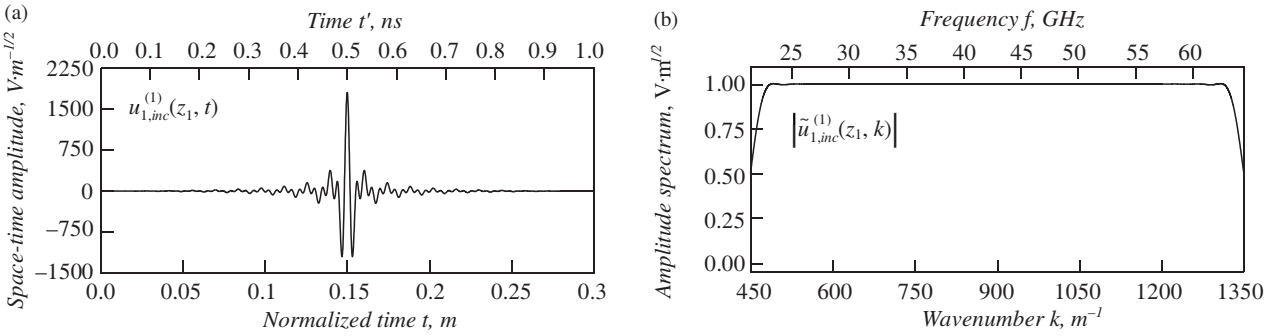

FIGURE 5. (a) Time profile of the space-time amplitude of the primary wave exciting the radiator; (b) its amplitude spectrum.

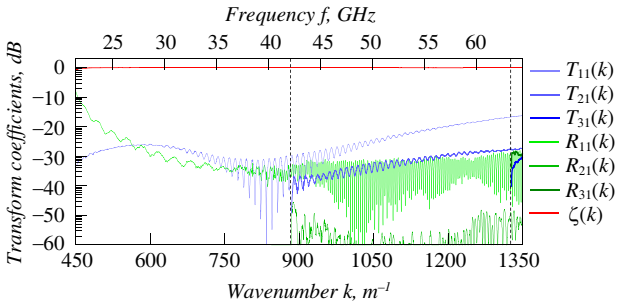

FIGURE 6. Transformation coefficients of the primary wave for the radiator shown in Fig. 4 when excited from the port I. Dielectric objects are assumed lossless.

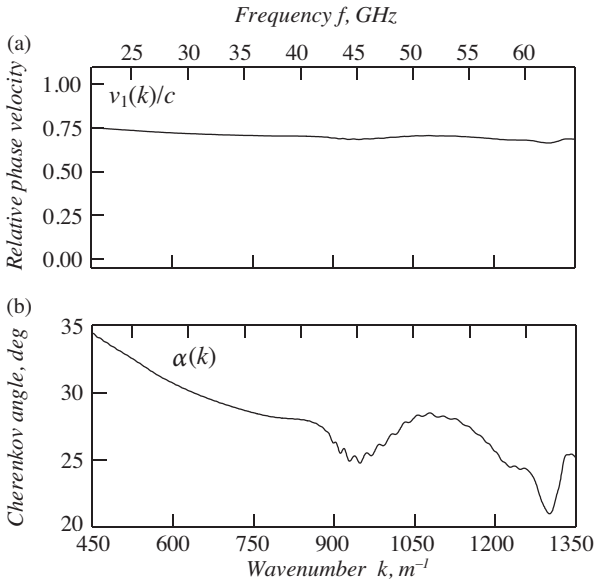

FIGURE 7. (a) Computed relative phase velocity in the dielectric waveguide; (b) propagation angle of Cherenkov waves in the medium with ε_2.

According to the Cherenkov wave theory, the angle α between the propagation direction of Cherenkov waves and the primary wave's propagation direction is

$$\alpha = \arccos(v_2/v_1), \tag{23}$$

where v_1 is the phase velocity of the primary wave, and v_2 is the phase velocity of the wave in the medium where Cherenkov waves are generated. In our case, $v_2 = c/\sqrt{\varepsilon_2}$, and $v_1 = v_1(k)$ is the phase velocity of the wave in the dielectric waveguide. Since phase velocity v_1 depends on frequency (wavenumber), the Cherenkov angle of radiation is also frequency-dependent, $\alpha = \alpha(k)$. The function $v_1(k)$ does not have an exact analytical form but can be estimated through a separate numerical experiment [11]. We conducted such an auxiliary experiment by simulating the propagation of the pulse (19) on a regular section of the dielectric waveguide without prism $ABCD$. Using the kinematic approximation, it can be shown that [11]

$$v_1(k) = \frac{ck\Delta L}{\arg \tilde{E}_x(g_2, k) - \arg \tilde{E}_x(g_1, k)}, \tag{24}$$

where $g_1 = \{y, z_1\}$ and $g_2 = \{y, z_2\}$ are two observation points inside the waveguide with a distance $\Delta L = |z_2 - z_1|$ between them ($\Delta L < \lambda_{min}$; λ_{min} is the minimum wavelength in the working pulse spectrum); and $\tilde{E}_x(g, k)$ is the Fourier spectrum of the field at a fixed point g.

Figure 7 shows computed values of the relative (to the speed of light) phase velocity in the dielectric waveguide and Cherenkov angle α as functions of the wavenumber. The dependence $\alpha(k)$ predicts that Cherenkov waves will be radiated within a narrow sector, approximately 10 to 15 degrees wide. This prediction is confirmed by our numerical experiment. Within the prism and in the antenna near field, the radiated pulse exhibits recognizable wavefronts with a geometry close to planar. The angles β between these wavefronts and the z-axis vary for different parts of the pulse but remain close to each other. For the most intense part of the pulse (Fig. 4), this angle can be estimated as $\beta \approx 64.71°$. The condition $\alpha + \beta = 90°$ is satisfied for $k \approx 924\,\mathrm{m}^{-1}$ (Fig. 7(b)), which can be considered a good agreement between theoretical and numerical values.

After a Cherenkov wave is generated in a medium that is optically more dense than its surroundings, it can be emitted into free space. Its passage through such an interface inevitably leads to a reflection and loss of energy. This is a common drawback of dielectric antennas, though its impact can be minimized. Fig. 8 plots the energy reflection coefficient [40]

$$R(\theta_i) = \left[\frac{\sqrt{\varepsilon_2}\cos\theta_i - \sqrt{1 - \varepsilon_2 \sin^2\theta_i}}{\sqrt{\varepsilon_2}\cos\theta_i + \sqrt{1 - \varepsilon_2 \sin^2\theta_i}}\right]^2 \tag{25}$$

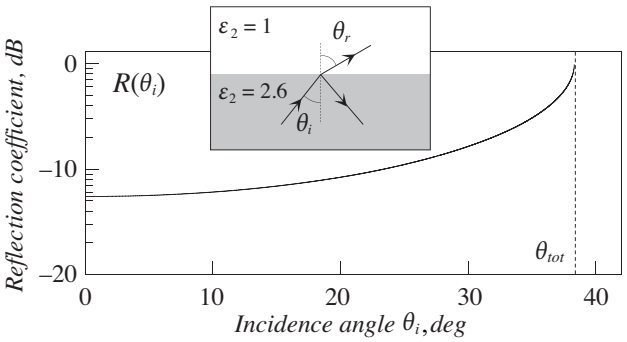

FIGURE 8. Reflection coefficient of a plane wave from the interface between the medium with ε_2 and vacuum as a function of the incidence angle. The angle of total internal reflection $\theta_{tot} = \arcsin\left(2.6^{-1/2}\right) \approx 38.33°$.

as a function of the incidence angle θ_i for a plane wave passing through the interface between the medium with ε_2 and free space. This function has a minimum at $\theta_i = 0$ ($R(0) \approx 0.055$), which suggests a radiator design where Cherenkov waves strike the boundary with free space at normal incidence. For the radiator with considered geometry (Fig. 4), $\theta_i \approx 45 - \alpha = \beta - 45 = 19.71°$, $R(\theta_i) \approx 0.083$, and the refraction angle $\theta_r = \arcsin\left(\sqrt{2.6}\sin\theta_i\right) \approx 32.7°$, which means the radiation occurs at approximately a $12.3°$ angle to the z-axis.

4. ANTENNA DESIGN

The data obtained in the previous section are sufficient for the model synthesis of a Cherenkov antenna with parameters suitable for practical applications. For it, we modify the radiator shown in Fig. 4 as follows. The angle at vertex C of the prism is set to $63°$, which approximately corresponds to the middle of the range of angles α (Fig. 7(b)) predicted by the theory for the band $\tilde{k}_1 < k < \tilde{k}_3$. The angles at vertices B and D remain unchanged. Additionally, face AB is covered with metal to suppress side lobes of the radiation pattern [11], and waveguide port II is removed, with the corresponding cross-section of the dielectric waveguide also being covered with metal.

The general view of the antenna is shown in Fig. 9(a). Simulating its excitation with the pulse (19) allowed us to calculate its radiation pattern $D(\phi, k)$ within the range $450 < k < 1350\,\mathrm{m}^{-1}$, Fig. 9(b), and reflection coefficients $R_{11}(k)$ and $R_{21}(k)$ of the primary TE_1 wave in the feeding waveguide, taking into account ohmic losses in the dielectric elements, Fig. 9(c). The radiation pattern exhibits a single dominant main lobe at frequencies above 26 GHz, with its direction $\bar{\phi}$ slowly decreasing as k increases. This behavior of $D(\phi, k)$ and radiation efficiency $\zeta(k) = 1 - R_{11}(k) - R_{21}(k)$ confirms the preliminary conclusions drawn in the previous section: the Cherenkov antenna is capable of radiating a broad spectrum of wavelengths into a narrow angular sector with high efficiency. This specific property enables the antenna to emit (and receive) pulses with a duration significantly smaller than its longitudinal dimensions (Fig. 4 and Fig. 9(a)).

The horizontal dashed line in Fig. 9 marks the angle $\phi = 90° - 63° = 27°$ coinciding with Cherenkov angle α, for which the prism geometry was adjusted. Due to the frequency dispersion of waves in the dielectric waveguide (Fig. 7(a)), the direction $\bar{\phi}$ of the main lobe of the radiation pattern exceeds this value in the low-frequency part of the considered range and falls below it in the high-frequency part. Thus, there is a weak monotonic divergence of waves with respect to k and ϕ. This suggests the use of a dielectric lens to improve the antenna's radiation pattern. A natural solution is to integrate such a lens with the prism where the Cherenkov wave is generated. This leads to an antenna design with a convex aperture, Fig. 9(d). The curvature radius R of this face was estimated using the geometric optics approximation: for the aperture size $\bar{D} \approx 110\,\mathrm{mm}$ and divergence angle $\Delta\phi \approx 35° - 20° = 15°$, the distance from the aperture to the center of curvature should be $R \approx \bar{D}/(2\sin\,(\Delta\phi/2)) \approx 421\,\mathrm{mm}$. In our model, we used $R = 400\,\mathrm{mm}$.

The computed radiation pattern of this antenna is shown in Fig. 9(e), and the reflection coefficients of the TE_1 wave are presented in Fig. 9(f). As expected, the dependence of the main lobe direction $\bar{\phi}$ on k became closer to the constant value $\bar{\phi}(k) = 27°$; however, its width increased.

A more precise energy balance calculation for the antenna with convex aperture, based on time-integrating the Poynting vector fluxes (16) through the virtual boundaries $\mathbf{L}_1$ and $\mathbf{L}$, performed for primary, reflected, and radiated waves (indexes "inc", "$refl$", and "rad"), reveals that the fractions of radiated (η_{rad}), reflected (η_{refl}), and lost in the dielectric elements (η_{loss}) energy are

$$\eta_{rad} = \frac{W_{\mathbf{L},rad}}{W_{\mathbf{L}_1,inc}} \approx 0.938,$$

$$\eta_{refl} = \frac{W_{\mathbf{L}_1,refl}}{W_{\mathbf{L}_1,inc}} \approx 0.021, \tag{26}$$

$$\eta_{loss} = \frac{W_{\mathbf{L}_1,inc} - W_{\mathbf{L},rad} - W_{\mathbf{L}_1,refl}}{W_{\mathbf{L}_1,inc}} \approx 0.041.$$

Here, for brevity, the argument t of $W_{\ldots}(t)$ functions is omitted. All calculations were performed for a time value of $t = 2.55\,\mathrm{m}$ (or 8.5 ns). This time interval is sufficient to ensure that almost all of the energy has left the analysis domain. A similar ratio is observed for the antenna with planar aperture.

Figure 10 shows the amplitude spectra of the radiated wave measured at five equally spaced observation points, P_1 to P_5. These points are located 25 mm apart and 2 mm from the planar aperture of the antenna, see Fig. 9(a). These dependencies indicate a nonuniform spatial-frequency distribution of energy in the radiated pulse. Although all frequency components of the primary pulse were radiated with high efficiency in approximately the same direction (Fig. 9(b)), their energy distribution differs in the transverse direction (relative to the wave vector). This is due to both the dispersion of the phase velocity in the dielectric waveguide and the varying degree of penetration of waveguide waves into the scattering prism. The latter factor causes low-frequency components of the primary pulse, which have larger evanescent portion outside the dielectric waveguide, to transform into Cherenkov waves faster than

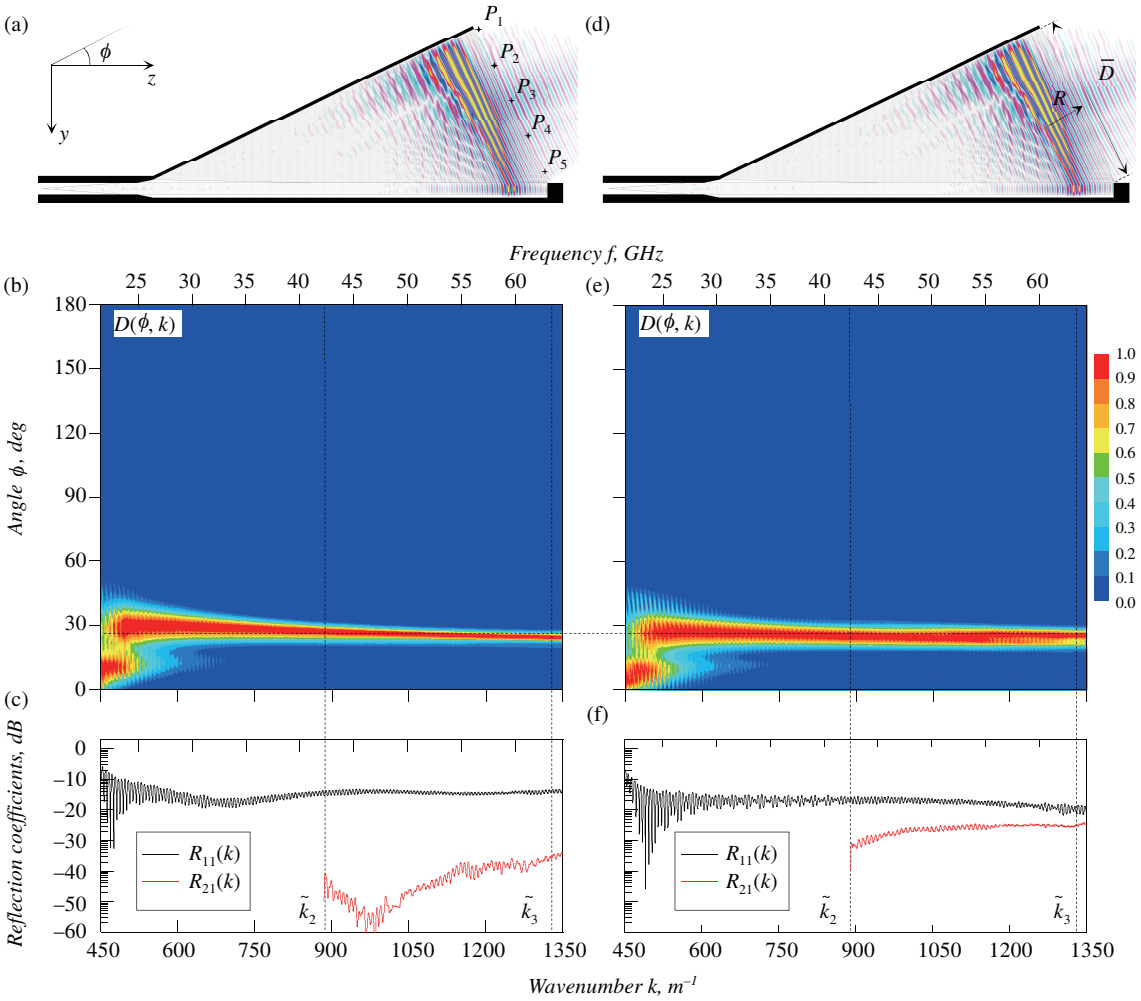

FIGURE 9. (a) General view of the synthesized Cherenkov antenna with planar aperture; (b) its radiation pattern $D(\phi, k)$; (c) reflection coefficients of the primary TE_1 wave into the feeding waveguide. Fragments (d)–(f) show the same characteristics for the antenna with convex aperture. In fragments (a) and (d), the distribution of E_x component in the computation domain is shown for the instant of time $t' = 2$ ns. Losses in dielectric objects were taken into account.

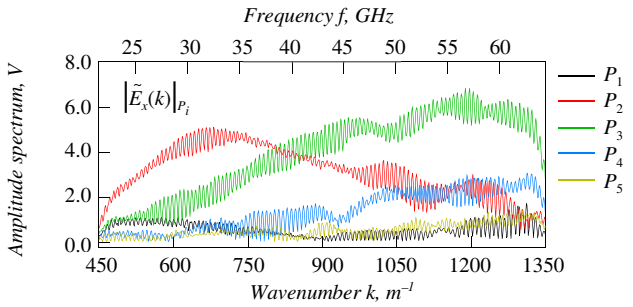

FIGURE 10. Spectrum of the radiated field at five observation points $P_1, \ldots, P_5$ near the antenna aperture (see Fig. 9(a)).

high-frequency components. These processes can be controlled by adjusting the geometry of the gap between the dielectric waveguide and the prism.

Figure 11 presents the radiation pattern of the antenna with convex aperture at 40 GHz, along with the distribution of the electric field component in the computation domain at two different instants of time. This is observed when the antenna is excited by a narrowband pulse

$$u^{(1)}_{n,inc}(z_1, t) = 4 \cdot S(t) \cdot \cos\big(k_c(t - T)\big), \tag{27}$$

where envelope $S(t)$ is defined by (20) and

$$\tilde{x}(t) = \begin{cases} (t - t_0)/(t_1 - t_0), & t_0 \le t \le t_1 \\ 1, & t_1 < t < t_2 \\ (t - t_3)/(t_2 - t_3), & t_2 \le t \le t_3 \\ 0, & t < 0,\ t > t_3 \end{cases}, \tag{28}$$

$t_0 = 0$, $t_1 = 0.02$ m, $t_2 = 2.98$ m, $t_3 = 3$ m (pulse duration 10 ns), $k_c = 838.33801\,\mathrm{m}^{-1}$ ($f = 40$ GHz). Fig. 11(b) illustrates the efficiency of energy transfer from the dielectric waveguide into the prism. The intensity of the primary traveling wave decreases significantly as it propagates through the section of the waveguide adjacent to the dielectric prism. As a result, the field amplitude in the waveguide near the antenna aperture is reduced to just a few percent of the wave's amplitude in the feeding port.

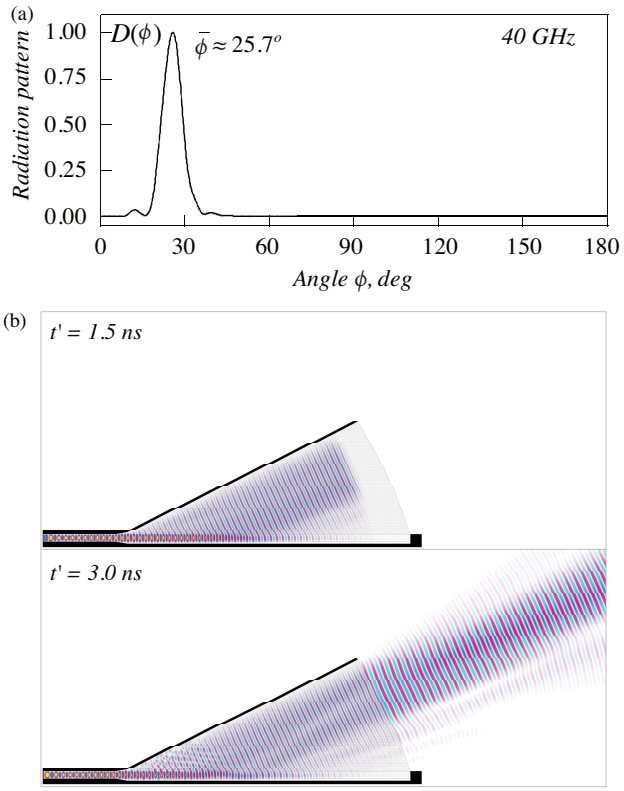

FIGURE 11. (a) Radiation pattern of the antenna with convex aperture at 40 GHz. (b) Distribution of E_x component in the computation domain at 1.5 and 3 ns.

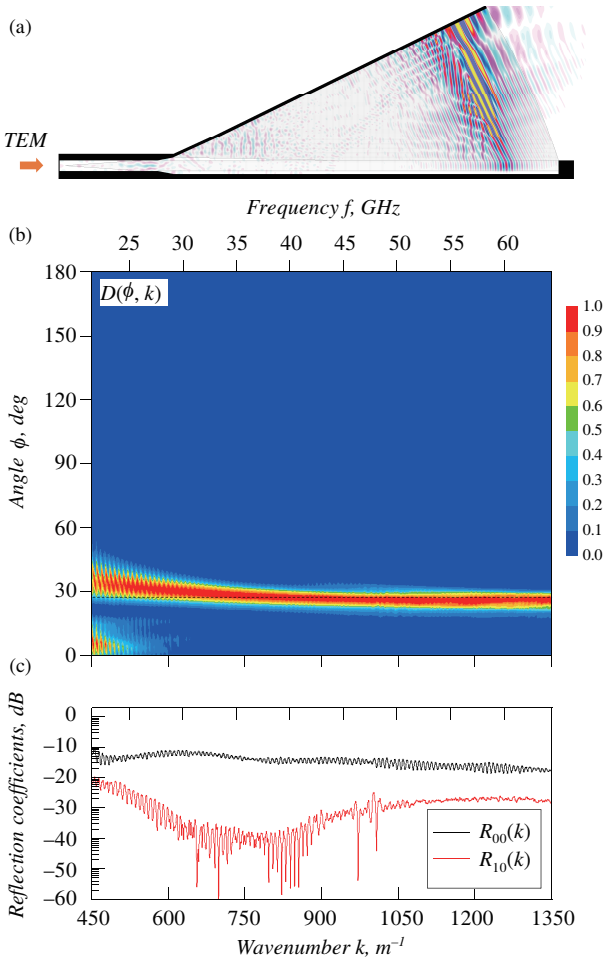

FIGURE 12. Excitation of the Cherenkov antenna with TEM pulse. (a) Distribution of H_x component in the computation domain at the instant of time $t' = 2$ ns; (b) radiation pattern of the antenna; (c) reflection coefficients of the primary wave.

The independence of the Cherenkov wave generation mechanism from polarization suggests that the characteristics of the synthesized radiator (radiation pattern, efficiency) for H-waves should be approximately the same as for E-waves, which is confirmed by numerical experiments.

Figure 12 presents the results of numerical modeling of the antenna with convex aperture (Fig. 9(d)) when it is excited by the TEM-pulse (19) from port I (problem (2), with $n = 0$ and dielectric losses included). The calculated radiation pattern $D(\phi, k)$ (Fig. 12(b)) is similar to the one obtained for E-waves (Fig. 9(e)). The reflection coefficient (Fig. 12(c)) of the primary wave back into port I is slightly higher than that for E-waves, but remains below approximately 0.08 across the entire frequency range considered. This value can be reduced through further optimization of the antenna geometry and its matching to the feeding waveguide port. A more detailed comparison of the radiation patterns $D(\phi)$ for E- and H-waves at various frequencies (Fig. 13) reveals their differences.

At sufficiently low frequencies, where the influence of the prism and metal substrate on the evanescent part of the waveguide wave is significant, notable differences may arise in both direction and width of the main lobe of radiation pattern for two different polarizations. However, with increasing frequency, these differences diminish, and at certain frequencies, the directions of the main lobes for both polarizations, $\bar{\phi}_E$ and $\bar{\phi}_H$, become nearly identical. This behavior reflects the fact that with decreasing wavelength, a larger proportion of the waveguide wave becomes concentrated within the dielectric waveguide, and its phase velocity approaches the constant value $c/\sqrt{\varepsilon_1}$ for both polarizations.

The similarity between the radiation patterns for E- and H-waves, combined with the high radiation efficiency, suggests that the considered Cherenkov-type antenna, once its design is extended to three-dimensional space, will be capable of efficiently and directionally emitting and receiving pulses with circular and elliptical polarizations. Our experience with leaky wave antennas (conceptually similar to the antennas discussed here) shows [41] that extending the 2D model of such a radiator to 3D does not lead to drastic changes in its basic characteristics. The change in the direction of the main lobe of the radiation pattern can be about 7 degrees while maintaining its width and high antenna efficiency. A similar behavior can be expected for Cherenkov-type antennas.

5. BEAM STEERING

In this section, we explore the feasibility of implementing beam steering for Cherenkov-type antennas.

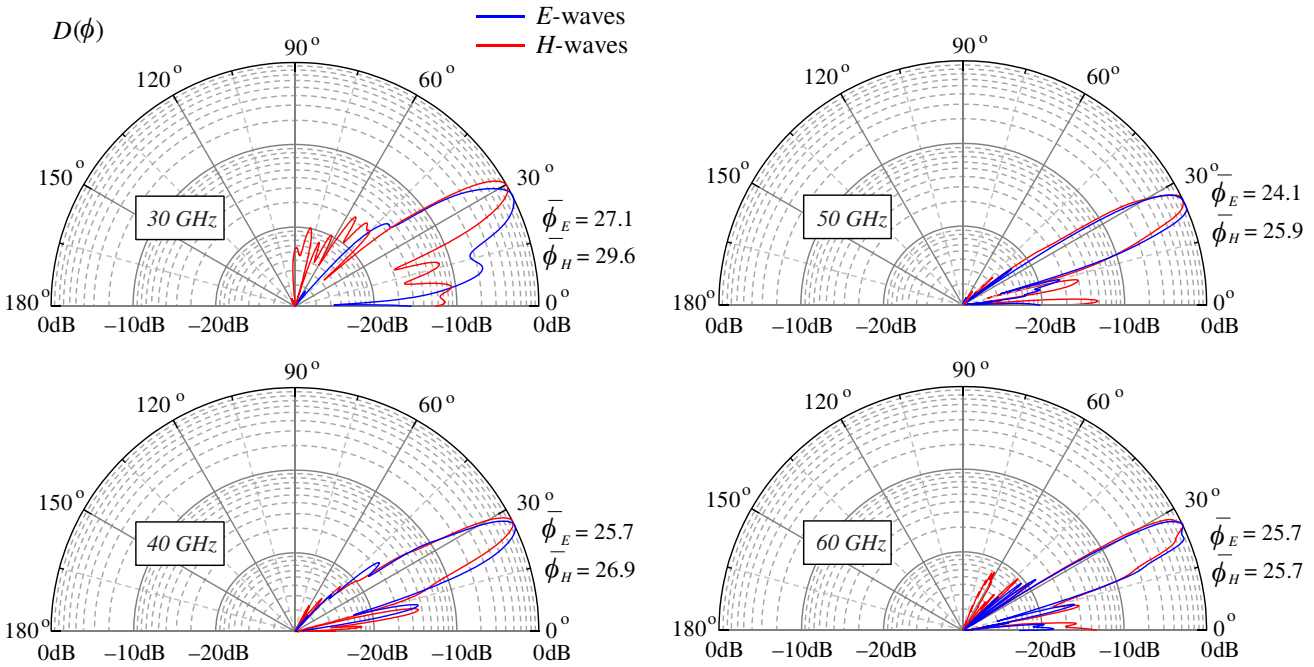

FIGURE 13. Radiation pattern of the antenna with convex aperture for two polarizations at four different frequencies.

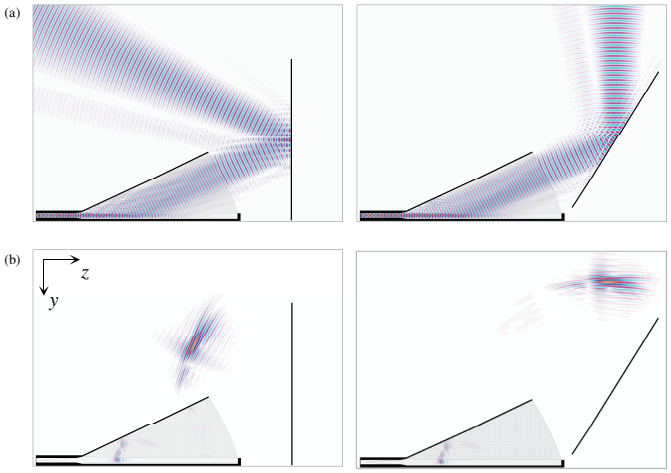

FIGURE 14. Control of (a) monochromatic and (b) pulsed radiation of the antenna using a flat mirror. The field distributions in fragment (b) correspond to the instant of time 3.1 ns.

First, it is worth noting that the radiation pattern of the antennas discussed in the previous sections can be easily manipulated using additional scatterers. For example, Fig. 14 presents results of numerical experiments demonstrating the control of both monochromatic (Fig. 14(a)) and pulsed (Fig. 14(b)) radiations by means of a flat metal mirror that can be rotated around its center. The mirror's width is 260 mm, and the angle between the mirror and z-axis was set to 90° and 57.6°. The latter value corresponds approximately to vertical (along the y-axis) propagation of the emitted wave. The wave (27) was used for monochromatic excitation at $f = 40$ GHz, while the wave (19) with parameters $n = 1$, $t_0 = 0$, $t_1 = 0.3$ m, $T = (t_0 + t_1)/2$, $k_c = 975\,\mathrm{m}^{-1}$, and $k_s = 325\,\mathrm{m}^{-1}$ was used for pulsed excitation. The bandwidth of such a pulse spans approximately one octave, $31.01 < f < 62.03$ GHz.

Beyond this apparent method, Cherenkov antennas offer a more elegant solution for beam steering. The dependence (23) of the Cherenkov angle α on the phase velocity v_1 of the primary wave in the open waveguide enables control of the radiation pattern by varying v_1 through an external control signal. This variation in v_1 can be achieved by tuning the permittivity of the dielectric waveguide. This, in turn, necessitates the use of tunable dielectrics [42], i.e., materials whose permittivity can be altered under the influence of an external electric or magnetic field (e.g., liquid crystals, nonlinear dielectrics, etc.)

In our model, we investigated characteristics of the Cherenkov radiator under variation of the permittivity of the dielectric waveguide, without specifying the material it could be made from. The radiator's geometry is identical to that shown in Fig. 4, except that port II was removed, and the waveguide was terminated with a metal wall (0.5 mm thick) at the cross-section containing the prism vertex C. In numerical simulations, the value of permittivity ε_1 varied from 1 (no dielectric waveguide present) to 2.6 (the dielectric waveguide becomes effectively merged with the scattering prism).

Figure 15 presents the results of numerical experiments for four different values of ε_1. Fig. 15(a) shows the distribution of electric field component E_x in the computation domain at the instant of time $t' = 1.7$ ns for different values of ε_1. The propagation speed of the primary pulse along the dielectric waveguide depends on ε_1, which leads to different inclinations of Cherenkov wavefronts relative to the longitudinal axis. Combined with the monotonic dependence of the phase velocity in the waveguide on the permittivity, $v_1 = v_1(\varepsilon_1)$, that results in a monotonic shift of the radiation pattern $D(\phi, k)$ along the coordinate ϕ as ε_1 changes, see Fig. 15(b).

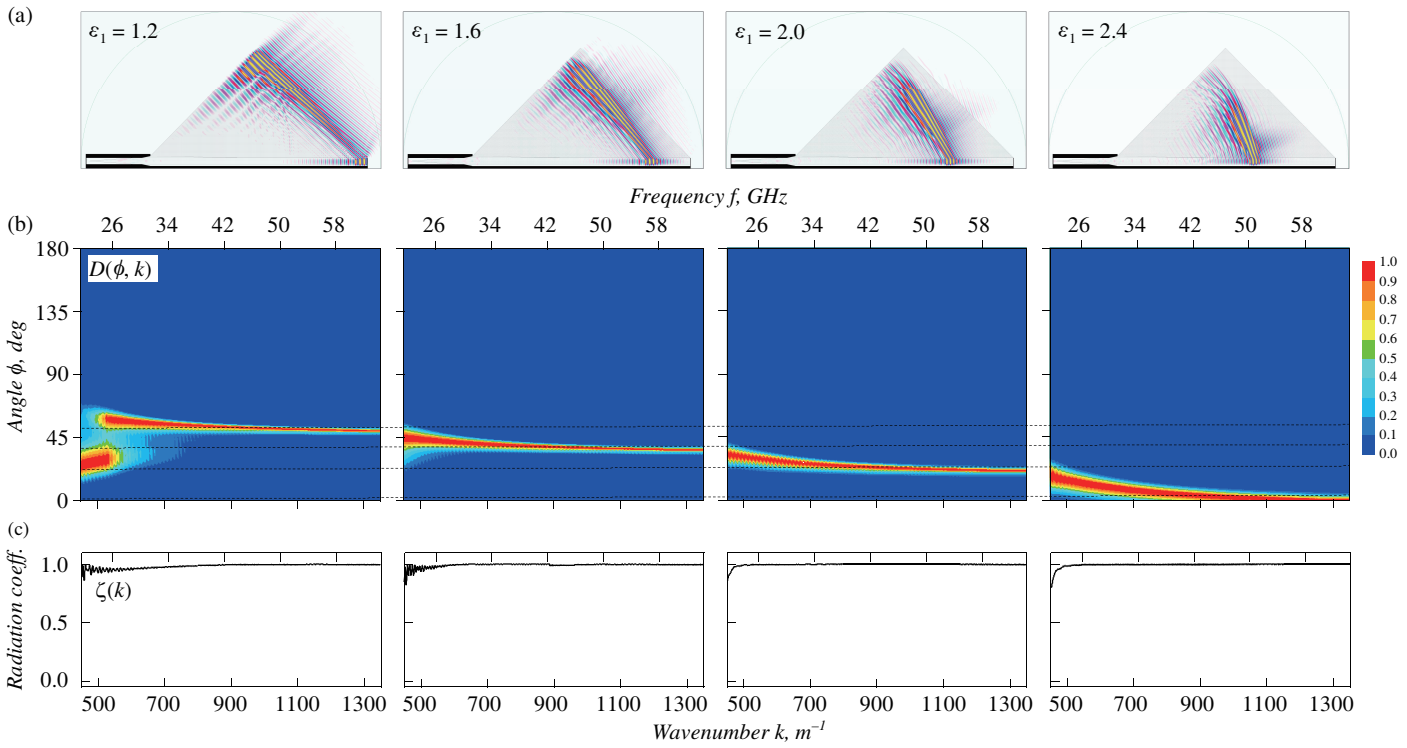

FIGURE 15. Spatial-energy characteristics of the Cherenkov antenna for four different values of ε_1 under excitation by the ultra-wideband pulse (19). (a) Distributions of the electric field component in the computation domain at the instant of time $t' = 1.7$ ns; (b) radiation patterns; (c) radiation coefficients. The horizontal dashed lines in fragment (b) indicate the main lobe directions $\bar{\phi} = 52.6°, 38.4°, 23.3°$, and $3.2°$ at $k = 900\,\mathrm{m}^{-1}$.

All four radiators demonstrate high efficiency across the entire frequency range under study, see Fig. 15(c). However, for lower values of ε_1 ($\varepsilon_1 \approx 1.5$ and below), our simulations revealed an effect of incomplete energy transfer from the primary pulse into the dielectric prism. For such ε_1, the phase velocity of the primary wave becomes so high that the pulse does not have enough time to completely transform into outgoing Cherenkov waves. As a result, a portion of the pulse reaches the metal wall located in the cross-section of the dielectric waveguide and diffracts there. This undesired effect can be mitigated by increasing the interaction length between the primary wave and scattering prism, that is, by extending the prism along the z-axis.

Another interesting effect observed for small values of ε_1 is an abrupt change in direction $\bar{\phi}$ of the main lobe of the radiation pattern $D(\phi, k)$ in the low-frequency region of the investigated range. For $\varepsilon_1 = 1.2$, this jump in $\bar{\phi}$ occurs near $k \approx 527\,\mathrm{m}^{-1}$. Importantly, this is not a threshold effect, but rather a continuous (albeit rapid) change in the radiation pattern's structure. At $k \approx 527\,\mathrm{m}^{-1}$, the pattern $D(\phi)$ exhibits a split main lobe with two dominant peaks, both equal to 1, see Fig. 16. To the left and right of this wavenumber value, one of these peaks gradually diminishes, transforming into a side lobe, and the derivative $d\bar{\phi}/dk$ changes sign at this point. This behavior suggests an insight into the physics behind this abrupt change in $\bar{\phi}$.

At sufficiently high values of k and ε_1, the primary wave's energy is relatively well confined within the dielectric waveguide, and the normal dispersion of such waveguides is observed ($dv/d\omega < 0$, Fig. 7(a)). For this reason, in the region

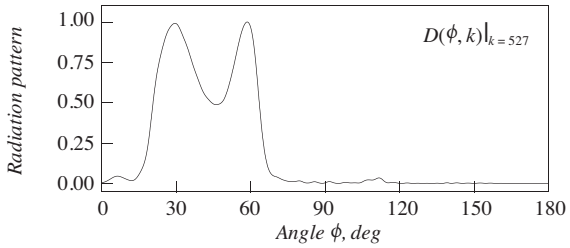

FIGURE 16. Radiation pattern for $\varepsilon_1 = 1.2$ and $k = 527\,\mathrm{m}^{-1}$.

of high values of k, $d\bar{\phi}/dk < 0$. As the permittivity ε_1 decreases, the angle of total internal reflection at the dielectric-air interface increases, which leads to an increase in the cut-off frequency of the dielectric waveguide's fundamental mode and causes the energy to be confined within the region bounded by the metal wall and adjacent faces of the prism. The wave structure in this waveguide channel resembles that of classic hollow metal waveguides with anomalous dispersion ($dv/d\omega > 0$, [43]), which results in a larger Cherenkov angle at higher frequencies, meaning $d\bar{\phi}/dk > 0$.

6. CONCLUSION

The findings from our study lead to the following conclusions. The Cherenkov mechanism for transferring electromagnetic energy from an optically less dense waveguiding medium to a more dense one enables the design of highly efficient antennas. These antennas provide the directional emission of pulses

of two orthogonal polarizations within a narrow sector and over a frequency band that can exceed one octave. Such Cherenkov-type antennas feature a simple design based on "open waveguide + dielectric prism" configuration and exhibit radiation patterns that are only weakly dependent on frequency. In one of the Cherenkov antenna models examined in this study (Fig. 9), the change in the direction of the main lobe of its pattern across the 30–60 GHz frequency range was $4.3°$ for the planar aperture and $1.5°$ for the convex one. Cherenkov antenna designs permit the electrical control of their parameters, including radiation patterns, through variation of the phase velocity of open waveguide waves. A drawback of these radiators is the requirement for dielectric prisms with linear dimensions significantly exceeding the maximum wavelength in the spectrum of the emitted or received electromagnetic pulse. However, this requirement is not critical in the millimeter and submillimeter wavelength ranges. We believe that it is precisely within these frequency ranges, Cherenkov-type antennas will find their effective applications. It can also be expected that the use of metamaterials [44, 45] or photonic crystals [46], exhibiting the reverse Cherenkov effect, for the manufacture of scattering prisms could lead to antenna designs with unique characteristics.

ACKNOWLEDGEMENT

The authors acknowledge the financial support by the Federal Ministry of Education and Research of Germany in the program of "Souverän. Digital. Vernetzt". Joint project 6G-RIC, project identification number: 16KISK020K.

REFERENCES

[1] Čerenkov, P. A., "Visible radiation produced by electrons moving in a medium with velocities exceeding that of light," *Physical Review*, Vol. 52, No. 4, 378, Aug. 1937.

[2] Frank, I. and I. Tamm, "Coherent visible radiation of fast electrons passing through matter," *Comptes Rendus (Dokl.) Acad.Sci. URSS*, Vol. 14, 109–114, 1937.

[3] Tamm, I., "Radiation emitted by uniformly moving electrons," *Journal of Physics USSR*, Vol. 1, 439–454, 1939.

[4] Watson, A. A., "The discovery of Cherenkov radiation and its use in the detection of extensive air showers," *Nuclear Physics B — Proceedings Supplements*, Vol. 212–213, 13–19, 2011.

[5] Branger, E., S. Grape, S. J. Svärd, P. Jansson, and E. A. Sundén, "On Cherenkov light production by irradiated nuclear fuel rods," *Journal of Instrumentation*, Vol. 12, No. 06, T06001, Jun. 2017.

[6] Mc Larney, B., M. Skubal, and J. Grimm, "A review of recent and emerging approaches for the clinical application of Cerenkov luminescence imaging," *Frontiers in Physics*, Vol. 9, 684196, Jul. 2021.

[7] Zhang, L., H. Xu, and W. Liu, "Inverse Cherenkov dielectric laser accelerator with alternating phase focusing for subrelativistic particles," *Physical Review Accelerators and Beams*, Vol. 27, No. 11, 110401, 2024.

[8] Hertel, T. W. and G. S. Smith, "Pulse radiation from an insulated linear antenna: An analogue of Cherenkov radiation from a moving charge," in *IEEE Antennas and Propagation Society International Symposium. 1998 Digest. Antennas: Gateways to the Global Network*, Vol. 2, 964–967, Atlanta, GA, USA, Jun. 1998.

[9] Hertel, T. W. and G. S. Smith, "Pulse radiation from an insulated antenna: An analog of Cherenkov radiation from a moving charged particle," *IEEE Transactions on Antennas and Propagation*, Vol. 48, No. 2, 165–172, Feb. 2000.

[10] Melezhik, P. N., M. Ney, S. S. Sautbekov, Y. Sirenko, A. A. Vertiy, and N. P. Yashina, "Directional antenna based on the Vavilov-Cherenkov radiation," *Telecommunications and Radio Engineering*, Vol. 75, No. 12, 1051–1056, 2016.

[11] Melezhik, P., M. Ney, S. Sautbekov, K. Sirenko, Y. Sirenko, A. Vertiy, and N. Yashina, "Cherenkov radiation based antenna with the funnel-shaped directional pattern," *Electromagnetics*, Vol. 38, No. 1, 34–44, 2018.

[12] Sautbekov, S., K. Sirenko, Y. Sirenko, and A. Yevdokymov, "Diffraction radiation effects: A theoretical and experimental study," *IEEE Antennas and Propagation Magazine*, Vol. 57, No. 5, 73–93, Oct. 2015.

[13] Sirenko, Y., P. Melezhik, A. Poyedinchuk, S. Sautbekov, A. Shmat'ko, K. Sirenko, A. Vertiy, and N. Yashina, "Radiation of electromagnetic waves induced by electron beam passage over artificial material periodic interfaces," Chap. 5 in *An Essential Guide to Electrodynamics*, 169–206, Nova Science Publishers, 2019.

[14] Sirenko, Y., S. Sautbekov, N. Yashina, and K. Sirenko, "A new approach to formation and directed radiation of powerful short radio pulses," *IEEE Transactions on Plasma Science*, Vol. 50, No. 10, 3422–3433, Oct. 2022.

[15] Belonogaya, E. S., S. N. Galyamin, and A. V. Tyukhtin, "Short-wavelength radiation of a charge moving in the presence of a dielectric prism," *Journal of the Optical Society of America B*, Vol. 32, No. 4, 649–654, 2015.

[16] Tyukhtin, A. V., S. N. Galyamin, and V. V. Vorobev, "Peculiarities of Cherenkov radiation from a charge moving through a dielectric cone," *Physical Review A*, Vol. 99, No. 2, 023810, Feb. 2019.

[17] Tyukhtin, A. V., S. N. Galyamin, V. V. Vorobev, and A. A. Grigoreva, "Cherenkov radiation of a charge flying through the inverted conical target," *Physical Review A*, Vol. 102, No. 5, 053514, Nov. 2020.

[18] Galyamin, S. N. and A. V. Tyukhtin, "Cherenkov radiation of a charge in axicon-based dielectric concentrator," *Physical Review Accelerators and Beams*, Vol. 23, No. 11, 113001, Nov. 2020.

[19] Askaryan, G. A., "Cerenkov radiation and transition radiation from electromagnetic waves," *Soviet Physics JETP*, Vol. 15, No. 5, 943–946, Nov. 1962.

[20] Askar'yan, G. A., "Emission of radio waves upon modulation of an intense beam of light in a medium," *Soviet Physics JETP*, Vol. 18, No. 2, 441–443, Feb. 1964.

[21] Kuhn, R., *Mikrowellenantennen*, Veb Verlag Technik, 1964.

[22] Balanis, C. A., *Antenna Theory: Analysis and Design*, John Wiley & Sons, 2016.

[23] Unger, H.-G., *Planar Optical Waveguides and Fibres*, Clarendon Press, 1977.

[24] Bakunov, M. I., E. A. Mashkovich, M. V. Tsarev, and S. D. Gorelov, "Efficient Cherenkov-type terahertz generation in Si-prism-$LiNbO_3$-slab structure pumped by nanojoule-level ultrashort laser pulses," *Applied Physics Letters*, Vol. 101, No. 15, 151102, Oct. 2012.

[25] Bakunov, M. I., E. A. Mashkovich, and E. V. Svinkina, "Asymmetric Cherenkov radiation for improved terahertz generation in the Si-prism-coupled $LiNbO_3$ layer," *Optics Letters*, Vol. 39, No. 24, 6779–6782, 2014.

[26] Bakunov, M. I., E. S. Efimenko, S. D. Gorelov, N. A. Abramovsky, and S. B. Bodrov, "Efficient Cherenkov-type optical-to-terahertz converter with terahertz beam combining," *Optics Letters*, Vol. 45, No. 13, 3533–3536, 2020.

[27] Sirenko, Y., S. Strom, and N. P. Yashina, *Modeling and Analysis of Transient Processes in Open Resonant Structures: New Methods and Techniques*, Springer, 2007.

[28] Sirenko, K. and Y. Sirenko, "The exact absorbing conditions method in the analysis of open electrodynamic structures," Chap. 5 in *Electromagnetic Waves in Complex Systems: Selected Theoretical and Applied Problems*, 225–326, Springer, 2016.

[29] Sirenko, Y., V. Pazynin, K. Sirenko, and N. Yashina, "Exact absorbing conditions for initial boundary value problems of computational electrodynamics. A review," Chap. 3 in *A Closer Look at Boundary Value Problems*, 43–124, Nova Science Publishers, 2020.

[30] Sirenko, Y., "Exact 'absorbing' conditions in outer initial boundary-value problems of the electrodynamics of nonsinusoidal waves. Part 3: Compact inhomogeneities in free space," *Telecommunications and Radio Engineering*, Vol. 59, No. 1&2, 1–31, 2003.

[31] Sirenko, Y., "Exact 'absorbing' conditions in outer initial boundary-value problems of the electrodynamics of nonsinusoidal waves. Part 4: Pulse antennas," *Telecommunications and Radio Engineering*, Vol. 59, No. 3&4, 1–15, 2003.

[32] Sirenko, K., Y. Sirenko, and H. Bağcı, "Exact absorbing boundary conditions for periodic three-dimensional structures: Derivation and implementation in discontinuous Galerkin time-domain method," *IEEE Journal on Multiscale and Multiphysics Computational Techniques*, Vol. 3, 108–120, Jul. 2018.

[33] Sirenko, K., V. Pazynin, Y. K. Sirenko, and H. Bagci, "An FFT-accelerated FDTD scheme with exact absorbing conditions for characterizing axially symmetric resonant structures," *Progress In Electromagnetics Research*, Vol. 111, 331–364, 2011.

[34] Taflove, A. and S. C. Hagness, *Computational Electromagnetics: The Finite-Difference Time-Domain Method*, Artech House, 2000.

[35] Pazynin, V. L., S. S. Sautbekov, K. Y. Sirenko, Y. Sirenko, A. A. Vertiy, and N. P. Yashina, "Comparison of exact and approximate absorbing conditions for initial boundary value problems of the electromagnetic theory of gratings," *Telecommunications and Radio Engineering*, Vol. 77, No. 18, 1581–1595, 2018.

[36] Mittra, R. and S. W. Lee, *Analytical Techniques in the Theory of Guided Waves*, Macmillan, 1971.

[37] Felsen, L. B. and N. Marcuvitz, *Radiation and Scattering of Waves*, John Wiley & Sons, 1994.

[38] Whittaker, T., S. Zhang, A. Powell, C. J. Stevens, J. Y. C. Vardaxoglou, and W. Whittow, "3D printing materials and techniques for antennas and metamaterials: A survey of the latest advances," *IEEE Antennas and Propagation Magazine*, Vol. 65, No. 3, 10–20, Jun. 2023.

[39] Lamb, J. W., "Miscellaneous data on materials for millimetre and submillimetre optics," *International Journal of Infrared and Millimeter Waves*, Vol. 17, No. 12, 1997–2034, Dec. 1996.

[40] Born, M. and E. Wolf, *Principles of Optics*, Pergamon Press, 1968.

[41] Pazynin, V., F.-C. Lutz, K. Schäpers, F. Bette, A. Begimova, and W. Keusgen, "Leaky wave antenna with metal-dielectric reflective grating for microwave applications in the 24–28 GHz range," in *Proc. of IEEE AP-S International Symposium/North American Radio Science Meeting*, 2287–2290, Ottawa, Canada, Jul. 2025.

[42] Kong, L. B., S. Li, T. S. Zhang, J. W. Zhai, F. Y. C. Boey, and J. Ma, "Electrically tunable dielectric materials and strategies to improve their performances," *Progress in Materials Science*, Vol. 55, No. 8, 840–893, 2010.

[43] Southworth, G. C., "Principles and applications of waveguide transmission," *Bell System Technical Journal*, Vol. 29, No. 3, 295–342, 1950.

[44] Duan, Z., B.-I. Wu, J. Lu, J. A. Kong, and M. Chen, "Reversed Cherenkov radiation in a waveguide filled with anisotropic double-negative metamaterials," *Journal of Applied Physics*, Vol. 104, No. 6, 063303, Sep. 2008.

[45] Duan, Z., X. Tang, Z. Wang, Y. Zhang, X. Chen, M. Chen, and Y. Gong, "Observation of the reversed Cherenkov radiation," *Nature Communications*, Vol. 8, No. 1, 14901, 2017.

[46] Ney, M., K. Y. Sirenko, Y. Sirenko, H. O. Sliusarenko, and N. P. Yashina, "2-D photonic crystals: Electromagnetic models of the method of exact absorbing conditions," *Telecommunications and Radio Engineering*, Vol. 76, No. 3, 185–207, 2017.